

Formation of a condensate in two-dimensional turbulence on a sphere

Antonio Segalini and Erik Lindborg 0

(Received 18 February 2025; revised 19 July 2025; accepted 19 July 2025)

We simulate the formation of a condensate on a sphere, generated by an inverse energy cascade originating from a stochastic forcing at spherical harmonic wavenumber $l_f\gg 1$. The condensate forms as two pairs of oppositely signed vortices lying on a great circle that is randomly rotating in three dimensions. The vortices are separated by 90° and like signed vortices are located at opposite poles. We show that the configuration is the maximum energy solution to a Hamiltonian dynamical system with a single degree of freedom. An analysis in wavenumber space reveals that interactions between widely separated scales of motions dominate the formation process. For comparison, we also perform freely decaying simulations with random initial conditions and prescribed spectra. The late time solutions consist of four coherent vortices, similar to the solutions of the forced simulations. However, in the freely decaying simulations the vortex configuration is not stationary but exhibits periodic motions.

Key words: turbulence theory, turbulence simulation, vortex dynamics

1. Introduction

One of the most striking examples of self-organisation in a physical system is the formation of a condensate generated by a two-dimensional (2-D) inverse energy cascade. That such a condensate can form was predicted by Kraichnan (1967) and numerically confirmed by Smith & Yakhot (1994) and Chertkov *et al.* (2007) who simulated 2-D turbulence on a square domain with periodic boundary conditions and stochastic forcing at wavenumber $k_f \gg 1$. Musacchio & Boffetta (2019) showed that a condensate can also arise in a thin box with periodic boundary conditions. In two dimensions, there are two conserved quadratic quantities, energy and enstrophy (half the square of vorticity). Energy cascades

¹Department of Earth Sciences, Uppsala University, Villavägen 16, SE-75236 Uppsala, Sweden

²Department of Engineering Mechanics, KTH, Osquars backe 18, SE-10044 Stockholm, Sweden **Corresponding author:** Erik Lindborg, erikl@mech.kth.se

towards small wavenumbers and enstrophy towards large wavenumbers. The simulations revealed that a Kolmogorov energy spectrum, $E(k) \sim k^{-5/3}$, formed at $k < k_f$ during a transient period, consistent with theoretical predictions. When the energy cascade reaches wavenumber unity, corresponding to the size of the confinement, energy starts to pile up in the smallest wavenumbers, the spectrum steepens to $E(k) \sim k^{-3}$ and the flow organises into two vortices of opposite sign.

On a sphere, this process is best described in spherical harmonic space. On a plane, the eigenvalue of the Laplace operator applied to a Fourier mode is equal to $-k^2$, where $k = |\mathbf{k}|$ is the magnitude of the wavenumber vector. On a sphere with radius a, the eigenvalue of the Laplace operator applied to a spherical harmonic, Y_{l}^{m} , is equal to $-a^{-2}l(l+1)$, where l is the wavenumber specifying the order of the associated Legendre polynomial and m is the wavenumber specifying the number of harmonic oscillations in the azimuthal direction. In the spherical harmonic description, l is the wavenumber corresponding to k in the Fourier description, while m has a less obvious connection to scale and is therefore less important. In a landmark paper, Fjørtoft (1953) made a spherical harmonic decomposition of the vorticity field on a sphere and formulated an argument showing that energy will cascade towards small l and enstrophy towards large l in spherical harmonic space, where small l corresponds to large scales and large l to small scales in physical space. The spherical harmonic formulation was further developed by Tang & Orszag (1978) and Boer (1983). Lindborg & Nordmark (2022) showed that the theory can be formulated in complete analogy with the planar formulation developed by Kraichnan (1967), with l playing the same role on the sphere as k on the plane. Fourier modes exchange energy and enstrophy through nonlinear triad interactions, described by the function T(k, p, q), which is the energy transfer to k from p and q, with integration over all wavenumber vector triplets, $\{k, p, q\}$, that form a triangle with sides $\{k, p, q\}$ (Kraichnan 1967). The transfer of enstrophy to k from p and q is equal to $k^2T(k, p, q)$. Correspondingly, interactions between spherical harmonic modes, are described by G(l, n, s), which is the transfer of energy to l from n and s, corresponding to triplets of harmonics, $\{Y_l^m, Y_n^i, Y_s^j\}$, with summation over all $\{m, i, j\}$ (Lindborg & Nordmark 2022). The transfer of enstrophy is equal to $a^{-2}l(l+1)G(l, n, s)$. Using an elegant proof given by Silberman (1954), it can be shown that G is zero unless s + n + lis odd and |l-n| < s < l+n. The spectral energy flux across wavenumber l can be calculated as

$$\Pi_E(l) = \sum_{1$$

and the spectral enstrophy flux can be calculated as

$$\Pi_{\Omega}(l) = \sum_{1$$

As shown by Fjørtoft (1953), for each triad $\{p, n, s\}$ such that p < n < s, n either acts as a source or a sink of energy and enstrophy for p and s. He argued that the first type of interaction, where n acts as a source, is dominant. The first sums in (1.1) and (1.2) contain all triads where energy and enstrophy flow through l from n to s and the second sums contain all triads where energy and enstrophy flow through l from n to p. In a constant energy flux range at $l \gg 1$, the Kolmogorov form of the spherical harmonic energy spectrum is

$$E(l) = Ca^{2/3} |\Pi_E|^{2/3} l^{-5/3}, (1.3)$$

where C is a dimensionless constant that has the same value as the corresponding constant in the Fourier description. The energy spectrum is invariant with respect to rotations of the polar axis of the spherical harmonic system, as is G(l, n, s) (Lindborg & Nordmark 2022).

Unlike the planar case, a condensate on a sphere cannot form as a single pair of vortices. Two vortices of same sign can be ruled out, since mean vorticity over a sphere is zero. Two vortices of opposite sign, situated in opposite hemispheres, would generate a circulation around the corresponding polar axis in the same direction in each hemisphere. This can also be ruled out, since mean angular momentum with respect to any main axis is conserved and therefore must remain zero, if initially zero, implying that the energy in l=1 is zero. If the condensate on a sphere forms as a number of coherent vortices, just as the condensate on a plane, we can thus expect that it will consist of two pairs of vortices of opposite sign.

2. Numerical set-up

We perform numerical simulations of the vorticity equation on a sphere

$$\partial_t \omega + \boldsymbol{u} \cdot \nabla \omega = -\nu (\nabla^2 + 2/a^2)^8 \omega + \boldsymbol{e}_r \cdot (\nabla \times \boldsymbol{f}), \tag{2.1}$$

where $\omega = e_r \cdot (\nabla \times u)$ is the vorticity, u the non-divergent velocity, ν is hyperviscosity, f is a stochastic forcing and e_r is the radial unit vector. The viscous term is designed to conserve angular momentum, analogous the Navier–Stokes viscous term on a sphere, $\nu(\nabla^2 + 2/a^2)$, (Gilbert, Riedinger & Thuburn 2014; Lindborg & Nordmark 2022). The high order of the hyperviscosity ensures that it acts almost exclusively at the highest-order modes. For this reason, a hyperviscosity operator of the form $-\nu\nabla^{16}$ can also be used, without any change of the general results, which we have confirmed numerically.

Equation (2.1) is solved using of a pseudo-spectral code based on spherical harmonics, developed by the first author. The code employs full dealiasing with the 3/2 rule (Peyret 2002), triangular truncation between wavenumbers (Krishnamurti *et al.* 2006) and an efficient method to compute Legendre transforms developed by Ishioka (2018). A semi-implicit third-order Adams–Bashforth backward-differentiation (AB/BDI3) time advancement scheme is implemented (Peyret 2002) to reduce the computational cost by minimising evaluations of the nonlinear terms in the pseudo-spectral framework. The time step is adjusted adaptively to maintain numerical stability. The hyperviscous term is integrated exactly in time via the factor.

$$\alpha = \exp\left\{-\frac{v}{a^{2p}} \left[l(1+l) - 2\right]^p \Delta t\right\},$$
 (2.2)

so that the AB/BDI3 scheme will take the form

$$\omega^{+1} = \frac{6\alpha}{11} \left[3\omega^0 - \frac{3\alpha}{2}\omega^{-1} + \frac{\alpha^2}{3}\omega^{-2} - \Delta t(3Q^0 - 3\alpha Q^{-1} + \alpha^2 Q^{-2}) + \Delta t F^0 \right], \quad (2.3)$$

where the superscripts indicate the time step (0 is the current one and +1 is the next one), Q indicates the advective nonlinear term in (2.1) and F is the forcing term. The equation is solved for each spherical harmonic mode ω_l^m with corresponding nonlinear term Q_l^m and forcing term F_l^m . As (2.3) shows, the AB/BDI3 requires storing of two prior fields at earlier time steps and two precomputed nonlinear terms. Thus, only one evaluation of the nonlinear term is needed per time step, significantly reducing the computational cost compared with Runge–Kutta methods. The spherical harmonics transform is performed by combining the FFTW3 library (Frigo & Johnson 2005) for longitudinal Fast Fourier

Name	N_{lat}	N_{long}	l_{max}	l_f	ν	l_c
Run 1	256	512	170	100	1.83×10^{-35}	
Run 2	1024	2048	682	400	1.20×10^{-42}	
Run 3	256	512	170		1.83×10^{-35}	8
Run 4	1024	2048	682		1.20×10^{-42}	8
Run 5	256	512	170		1.83×10^{-35}	100

Table 1. Parameters of the simulations.

Transforms and the ISPACK library (Ishioka 2018) for meridional Legendre function transform (LXPACK). The code is written in Fortran 90 and it is parallelised by using the message passing interface standard.

The forcing is similar to the forcing used by Lindborg & Alvelius (2000) in Fourier space. It is white noise in time, has random phases and a narrow spectrum of the form $C \exp((l-l_f)^2/0.18)$, where the constant C is set so that the forcing injects energy at a prescribed rate, ϵ , which is set to unity. The enstrophy injection rate is then approximately equal to $l_f(l_f+1)$. As far as possible, the forcing is designed to be isotropic (directionally unbiased), by letting the magnitude of F_l^m be independent of m. In the limit of $l_f \to \infty$, such a forcing would be perfectly isotropic (Lindborg & Nordmark 2022). Since $l_f \gg 1$, it seems safe to assume that it is almost isotropic. For comparison, we also perform freely decaying simulations, initialised in a similar way as the simulations by Cho & Polvani (1996), with a random vorticity field conforming to a relatively narrow spectrum centred at $l = l_c$. We present two forced simulations, $\text{run}\{1, 2\}$, at resolution $l_{max} = \{170, 682\}$ and forcing wavenumber $l_f = \{100, 400\}$, both initialised from rest. We also present three freely decaying simulations, $\text{run}\{3, 4, 5\}$ at resolution $l_{max} = \{170, 682, 170\}$ and $l_c = \{8, 8, 100\}$. The simulation parameters are listed in table 1.

3. Results

3.1. Forced simulations

For a significant duration, the vorticity fields display only random fluctuation at the size of the forcing scale. This is seen in figure 1, $(a, \operatorname{run} 1)$ and $(c, \operatorname{run} 2)$, both from t = 10, where time is measured in units $e^{-1/3}a^{2/3}$. At $e^{-1/3}a^{2/3}$. At $e^{-1/3}a^{2/3}$. At $e^{-1/3}a^{2/3}$ are arrange themselves on a great circle with 90° separation and like signed vortices at opposite poles. In figure 1, $e^{-1/3}a^{2/3}$ and $e^{-1/3}a^{2/3}$, we see the four vortices in final states, where the vortex quartet is shown rotated to the equatorial plane. The great circle defining their configuration undergoes a random solid body rotation around the origin, with a characteristic velocity that is far slower than the typical fluid velocities. It may seem paradoxical that the circle moves in this way, since the mean angular momentum of the flow is zero, which is ascertained by the numerical method. Noting that the fluid velocity at the points defining the centres of the vortices is always zero, makes it less paradoxical. The circle is not a material line moving with the fluid, but moves as a solid body through the fluid which has no motion as a solid body. Animations of the vorticity fields in stereographic projections are available at Run1, Run2.

In figure 2(a,b), we see the time evolution of mean enstrophy. The cascades are set up at $t \sim l_f^{-2/3}$, after which enstrophy is quasistationary and then enters into a stage of slow growth. Also in this stage, the enstrophy growth is less than 1 % of the enstrophy

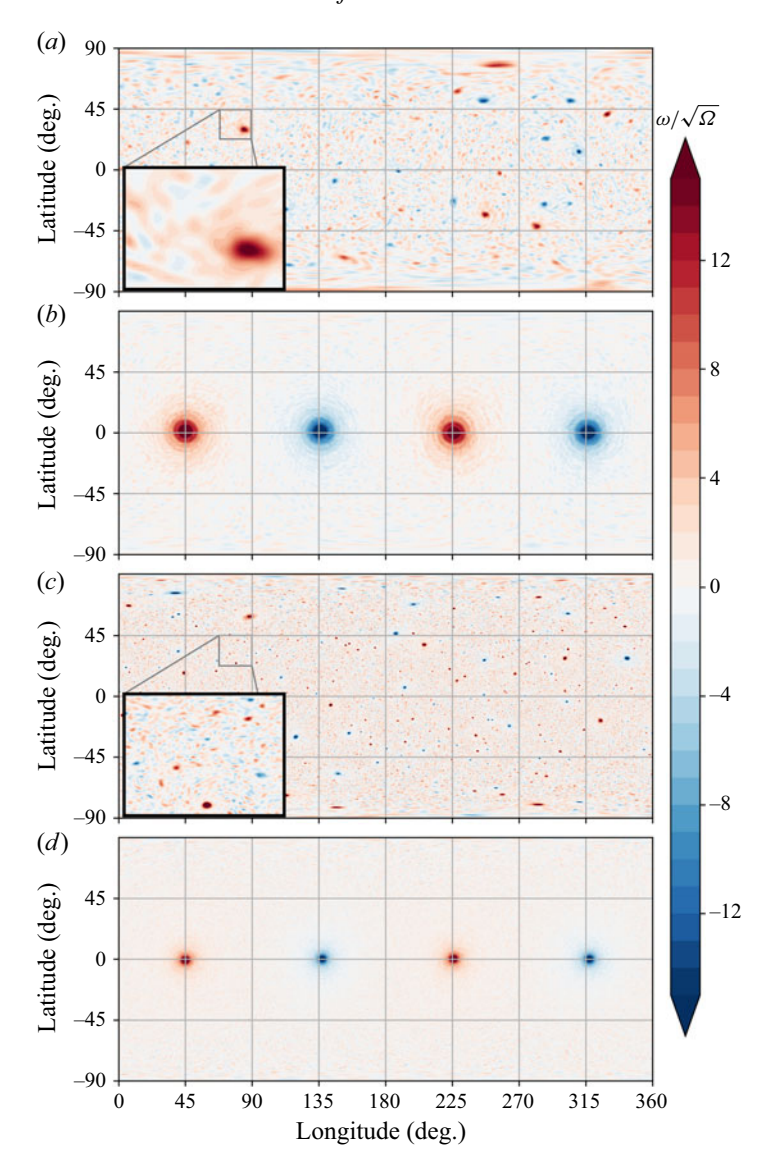


Figure 1. Vorticity fields. Run 1: (a) t = 10, (b) t = 1256; run 2: (c) t = 10, (d) t = 1067. In (b) and (d) the fields have been rotated so that the vortices lie on the equator.

injection, implying that virtually all injected enstrophy goes into a forward cascade. After the set up of the cascades, mean energy is growing at a constant rate which is close to 0.5 in both simulations, implying that approximately half of the injected energy is transferred to large wavenumbers where it is dissipated. In figure 2(c,d), we see the evolution of the compensated energy spectrum, $E(l)|\Pi_E|^{-2/3}l^{5/3}$, where $|\Pi_E|$ is taken as the energy growth. In the early stage, the spectra are similar to Fourier spectra from planar simulations (Smith & Yakhot 1994; Boffetta, Celani & Vergassola 2000; Chertkov *et al.* 2007), especially in run 1, where the Kolmogorov constant can be estimated as $C \approx 6$, indicated by a dashed line. In a later stage, energy accumulates in low wavenumbers of even order, leading to a zig-zag shaped spectrum with high/low energy in even/odd modes. This is first visible at l < 10 and subsequently appears at l > 10. The zig-zag spectrum is

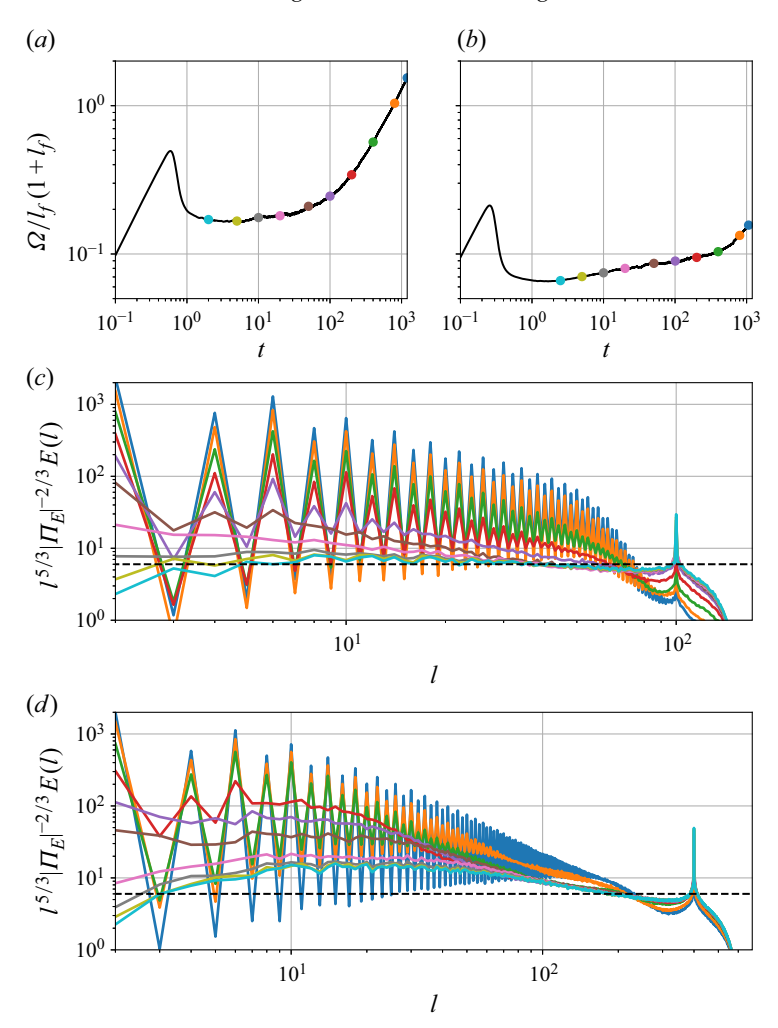


Figure 2. Mean enstrophy, Ω , normalised by $l_f(1+l_f)$ versus time; (a) run 1, (b) run 2. Evolution of compensated energy spectra; (c) run 1, (d) run 2. The colour of each spectrum is associated with the time where it is computed, as indicated in (a) and (b). The dashed lines in (c-d) indicate the Kolmogorov constant C=6.

a manifestation of the symmetric arrangement of the vortices. To see this, we expand the vorticity field in a spherical harmonic system whose polar axis coincides with the polar axis of the great circle of the configuration

$$\omega(\theta, \phi) = \sum_{l=1}^{l_{max}} \sum_{m=-l}^{l} \omega_l^m Y_l^m(\theta, \phi), \tag{3.1}$$

where θ is the colatitude and ϕ is the longitude. A symmetric configuration of four vortices of equal strength on the equator satisfies the symmetries $\omega(90^{\circ} + \theta, \phi) = \omega(90^{\circ} - \theta, \phi)$ and $\omega(\theta, \phi + 90^{\circ}) = -\omega(\theta, \phi)$. The spherical harmonics that satisfy these symmetries are those with $\{l = \text{even}, m = 2 + 4i\}$, where i is an integer. In figure 3, we see the enstrophy m-spectra from run 2 for (a) l = 2, 4, 6, 8, 10 and (b) l = 20, 30, 40. In both plots, essentially all enstrophy is found in m = 2 + 4i. A close inspection of figure 2 reveals that there is a secondary period in E(l), with extra strong peaks in l = 2 + 4i.

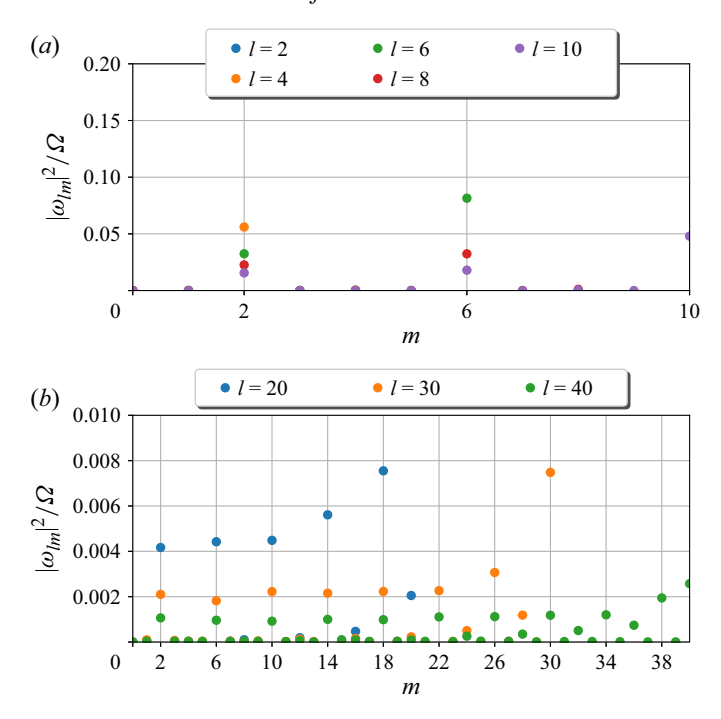


Figure 3. Azimuthal enstrophy spectra normalised by mean enstrophy, Ω , for different l from run 2 at t = 1067. Panels show (a) l = 2, 4, 6, 8, 10, (b) l = 20, 30, 40.

Clearly, the spherical harmonic energy spectrum of the condensate is very different from the continuous Fourier spectrum of the two coherent vortices in the condensate simulated by Chertkov *et al.* (2007). However, also in this case it can be argued that energy accumulates in certain modes, due to the overall symmetry, although this is not revealed by the Fourier spectrum, E(k), which only contains information of the averaged energy as a function of the magnitude, k, of the wavenumber vector k. A vorticity field of two coherent vortices of equal strength and opposite sign in a 2π -periodic domain, whose centres are located along a diagonal, obeys a symmetry of the form $\omega(x + \pi, y - \pi) = -\omega(x, y)$ (see figure 1c in Chertkov *et al.* 2007). All energy of such a field is contained in Fourier modes, $k = (k_x, k_y)$, satisfying $k_x + k_y = \text{odd}$, while there is no energy in modes satisfying $k_x + k_y = \text{even}$ (see Appendix A).

A striking feature of the spectra seen in figure 2(c,d) is the attenuation of energy close to l_f , which is most clearly seen in run 1 but is also seen in run 2. In the end state of run 1, the zig-zag spectrum is visible all the way up to $l = l_f$, where the energy content is one order of magnitude smaller than in the early stage. A similar attenuation of energy close to the forcing wavenumber is also seen in the Fourier energy spectrum of the end state of the simulation by Chertkov *et al.* (2007) (see their figure 3a), although it is not as strong as in the end state of our run 1. Most likely, had the simulation been continued, an equally strong attenuation would have been observed in the Fourier spectrum as in the spherical harmonic spectrum. The observation that energy is attenuated close to the forcing wavenumber suggests that the presence of the vortices qualitatively alters the way energy is transferred in wavenumber space. More specifically, it suggests that condensation is a process in which interactions between widely separated scales of motion play a crucial role. To investigate this, we divide the set of all triads into local, defined as n < 5p, where n is the middle and p the smallest wavenumber, and non-local, defined as the

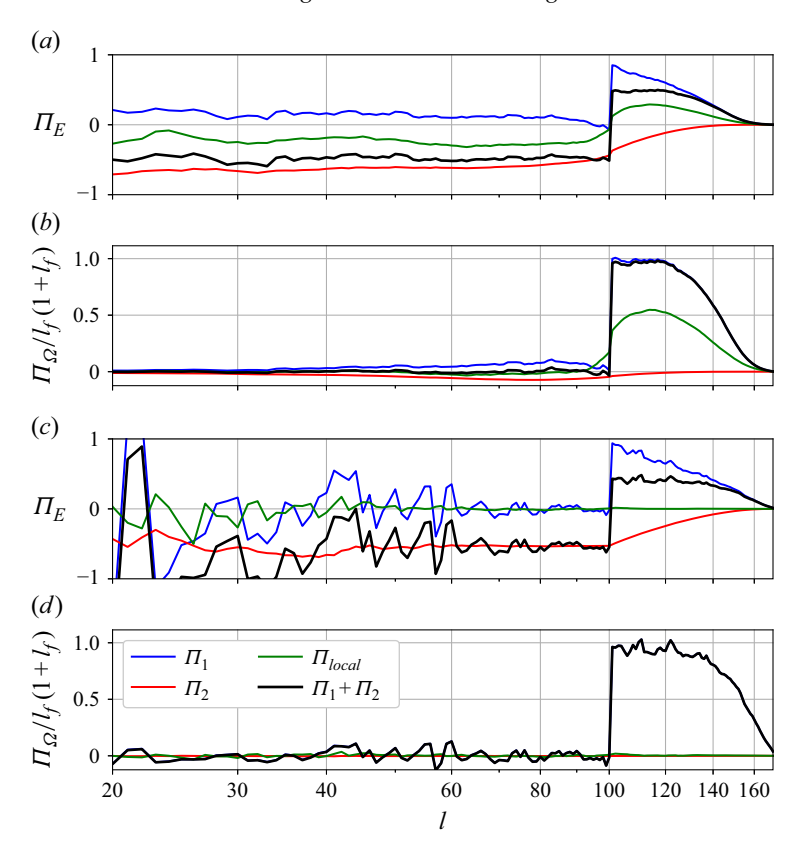


Figure 4. Energy and enstrophy fluxes from run 1. Panels show (a,b) t = 5; (c,d) t = 1256. Black: total fluxes. Blue: fluxes generated by the first sums in (1.1) and (1.2). Red: fluxes generated by the second sums. Green: fluxes generated by local triads.

complementary set. This is the same division of interactions into local and non-local as was introduced by Kraichnan (1971) in Fourier space. Then we use (1.1) and (1.2) to calculate the fluxes generated by each subset. Since each triad conserves both energy and enstrophy, the same is true for each subset. In figures 4 and 5(a,b) we see the energy and enstrophy fluxes at an early time, t = 5, from both simulations. The contributions from the first sums in (1.1) and (1.2), both denoted by Π_1 , are positive, while the contributions from the second sums, both denoted by Π_2 , are negative. This is in agreement with the prediction by Fjørtoft (1953) that the middle wavenumber in each triad interaction acts as a source of energy and enstrophy for the other two wavenumbers. At t = 5, the local energy and enstrophy fluxes are approximately half of the total fluxes close to l_f , while the local energy flux is less than half of the total at $l \sim 100$ in run 2 (figure 5a,b). This is in general agreement with predictions by Kraichnan (1971) and Chen et al. (2006) that non-local interactions are relatively strong in 2-D turbulence. During the formation of the condensate non-local interactions become increasingly dominant. In figures 4 and 5(c,d)we see the fluxes in the end states of the simulations. In run 1, the fluxes generated by the local triads are essentially zero in the end state, and in run 2 they are considerably smaller in the end state than in the early state. In particular, it is striking that there is such a weak contribution to the enstrophy flux. Since the enstrophy flux through l is generated by triads where $p < n < l \le s$, the flux through l is totally dominated by triads such that p < l/5.

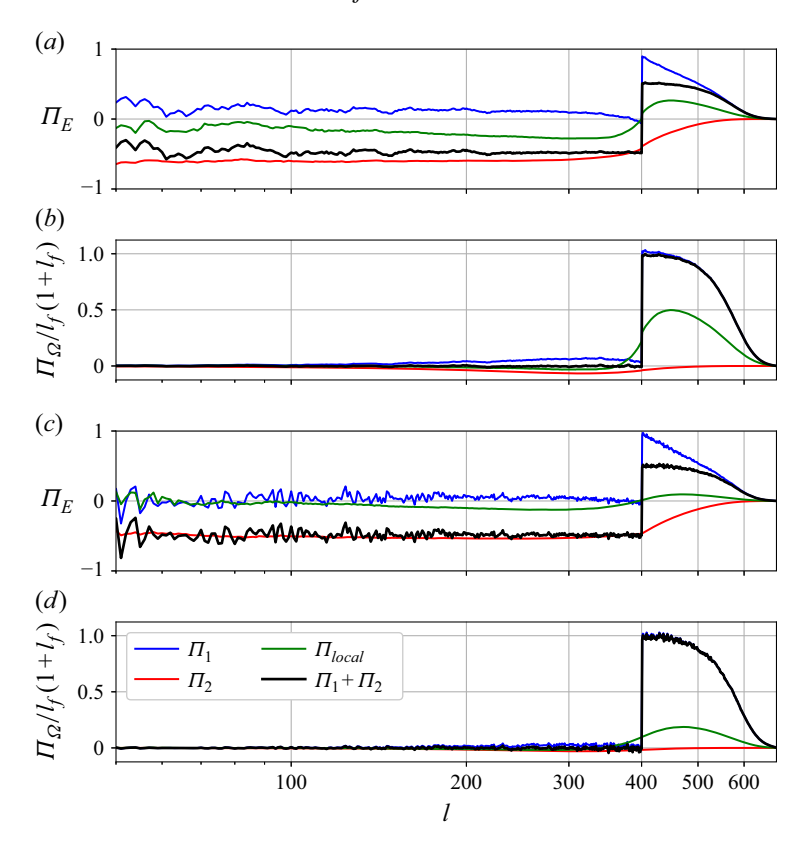


Figure 5. Energy and enstrophy fluxes from run 2. Panels show (a,b) t = 5; (c,d) t = 752. Black: total fluxes. Blue: fluxes generated by the first sums in (1.1) and (1.2). Red: fluxes generated by the second sums. Green: fluxes generated by local triads.

Thus, the condensate not only absorbs small-scale energy generated by the forcing, it also drains the flow from small-scale enstrophy.

In figure 6, we see the normalised mean vorticity profiles for the four vortices from both runs at t = 500 and t = 1000 and vorticity fields at these times. Kolokolov & Lebedev (2016) developed a theory for the structures of vortices that are generated by an inverse energy cascade that is balanced by large-scale friction. The theory is not applicable to our fields, since we have no large-scale friction. All of the four vortices are more or less equal in shape in both runs, and they are not wider at t = 1000 compared with t = 500. The width of the vortices in run 1 is approximately four times that of the vortices in run 2, reflecting the fact that l_f is four times larger in run 2 than in run 1. In the limit of large l_f , we can thus expect that the condensate would consist of four point vortices of equal strength, configured in the way we observe the vortices in our simulations. Indeed, this is a quite mysterious result. However, it is fully consistent with the simulations on a plane, exhibiting a Fourier energy spectrum $E(k) \sim k^{-3}$, which is the form of spectrum generated by two point vortices on a periodic plane (see Appendix A). We will not pretend to be able to explain why the condensate on the sphere consists of four point vortices of equal strength that are configured in this way. However, a comparison with some results derived from the theory of interacting point vortices on a sphere may provide some clues to an explanation.

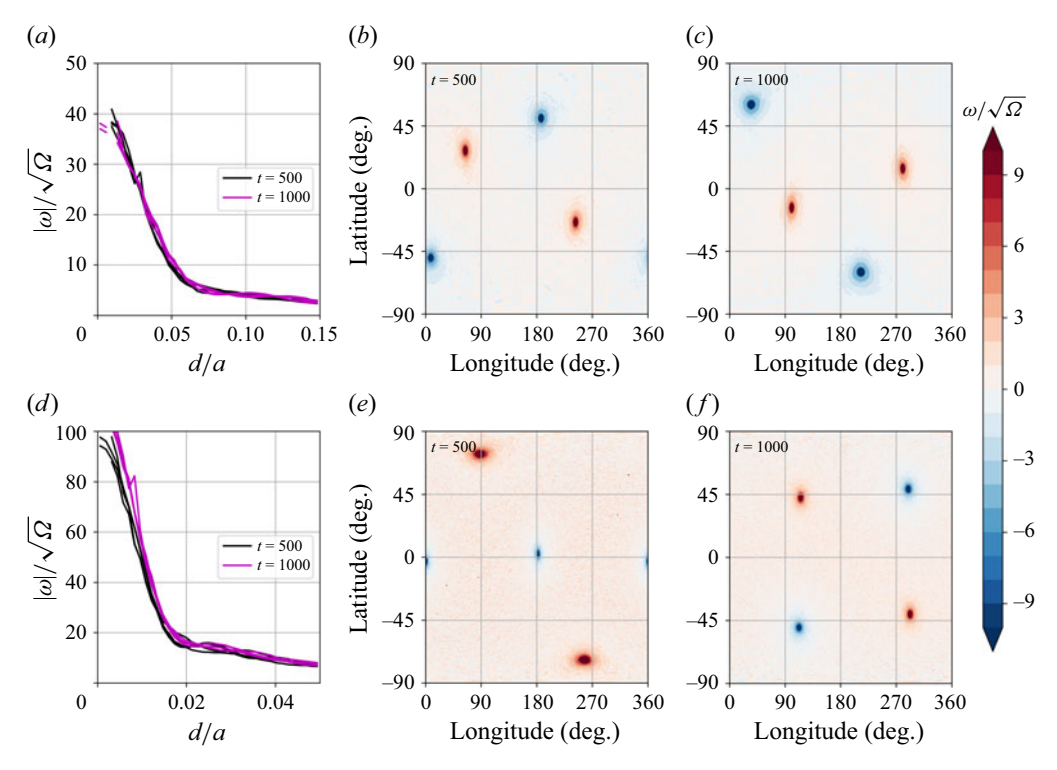


Figure 6. (a) Normalised vorticity as function of normalised distance from the vortex centre, for the four vortices at t = 500 (black) and t = 1000 (magenta) from run 1. (b,c) Vorticity field from run 1 at t = 500 and t = 1000. (d,e,f) Corresponding plots for run 2.

3.2. Four point vortices on a sphere

The classical theory of a dynamical system of point vortices on a plane (see Eyink & Sreenivasan 2006 for a review) was extended to a system of point vortices on a sphere by Polvani & Dritschel (1993). The theory has been applied to investigate the stability and equilibria of a system of four point vortices on a sphere (Dritschel 2020) and further extended to general curved surfaces (Dritschel & Boatto 2015). The equations of motion of a system of point vortices on the unit sphere can be written as

$$\boldsymbol{u}_{j} = \frac{\mathrm{d}\boldsymbol{n}_{j}}{\mathrm{d}t} = \sum_{i \neq j} \kappa_{i} \frac{\boldsymbol{n}_{i} \times \boldsymbol{n}_{j}}{1 - \boldsymbol{n}_{i} \cdot \boldsymbol{n}_{j}}, \qquad (3.2)$$

where n_i is the normal unit vector of the sphere at the position of the *i*th vortex and κ_i = is the strength of the *i*th vortex, which is related to its circulation, Γ_i , as $\kappa_i = \Gamma_i/4\pi$. The system (3.2) conserves angular momentum and energy defined as

$$L = \sum_{i} \kappa_{i} \mathbf{n}_{i}, \tag{3.3}$$

$$E = -\sum_{i \neq j} \kappa_i \kappa_j \ln(1 - \boldsymbol{n}_i \cdot \boldsymbol{n}_j), \tag{3.4}$$

and describes the motions of the point vortices in an inertial frame where the mean angular momentum of the flow is L and the energy is E. The energy can either can be interpreted as a potential energy of interaction between the point vortices or a kinetic energy of the

flow. The expression (3.4) can be deduced from the derivation found in Dritschel & Boatto (2015).

Since the position of each vortex is specified by two coordinates and the conservation laws provide four holonomic constraints, it appears that a system with k vortices has 2k-4 degrees of freedom. In the following, we develop a symmetry argument showing that the number is reduced to 2k-7 in the case L=0. In this case, the motion can only depend on how the vortices are configured relative to each other. To count the number of coordinates that are needed to specify such a configuration, fix the first vortex on the sphere. That leaves us with 2k-2 coordinates. However, one of these can be removed, because the whole configuration can be rotated around a main axis going through the point where we have fixed the first vortex, without changing the relative configuration. That leaves us with 2k-3 coordinates. The conservation laws provide four holonomic constraints. Thus, there are 2k-7 degrees of freedom. The four vortex system is thus the smallest possible, and this system has a single degree of freedom. In Appendix B, we formalise this argument. In the case $L \neq 0$, which corresponds to a rotating sphere where the flow has zero mean angular momentum, a similar symmetry argument shows that the numbers of degrees of freedom is 2k-5 and the smallest number of vortices is three.

The motion of the four vortex system with zero angular momentum can be represented by constant energy trajectories in a 2-D parameter space. Since the system has a single degree of freedom, there can be little doubt that such trajectories correspond to non-chaotic periodic motions. Extreme points, if they exist, correspond to stable and stationary solutions. To find the constant energy trajectories and possible extreme points of such a system we let (θ_i, ϕ_i) , i = 1, 2, 3, 4 be the coordinates of the vortices, where θ is the colatitude and ϕ is the longitude. As argued above, without loss of generality we can set $\theta_1 = \pi/2$, $\phi_1 = 0$ and $\theta_2 = \pi/2$. In Appendix B, we show that these coordinates specify the positions of the vortices in a rotating frame in which the first vortex is at rest and the second vortex has a single degree of freedom. The remaining five coordinates, ϕ_2 , θ_3 , ϕ_3 , θ_4 and ϕ_4 , are constrained by angular momentum and energy conservation, expressed as

$$\kappa_3 \cos \theta_3 + \kappa_4 \cos \theta_4 = 0, \tag{3.5}$$

$$\kappa_1 + \kappa_2 \cos \phi_2 + \kappa_3 \sin \theta_3 \cos \phi_3 + \kappa_4 \sin \theta_4 \cos \phi_4 = 0, \tag{3.6}$$

$$\kappa_2 \sin \phi_2 + \kappa_3 \sin \theta_3 \sin \phi_3 + \kappa_4 \sin \theta_4 \sin \phi_4 = 0, \tag{3.7}$$

$$E = -\kappa_{1}\kappa_{2} \ln(1 - \cos\phi_{2}) - \kappa_{1}\kappa_{3} \ln(1 - \sin\theta_{3}\cos\phi_{3}) - \kappa_{1}\kappa_{4} \ln(1 - \sin\theta_{4}\cos\phi_{4}) - \kappa_{2}\kappa_{3} \ln(1 - \sin\theta_{3}\cos(\phi_{3} - \phi_{2})) - \kappa_{2}\kappa_{4} \ln(1 - \sin\theta_{4}\cos(\phi_{4} - \phi_{2})) - \kappa_{3}\kappa_{4} \ln(1 - \cos\theta_{3}\cos\theta_{4} - \sin\theta_{3}\sin\theta_{4}\cos(\phi_{4} - \phi_{3})).$$
(3.8)

In figure 7(a), we plot the constant energy trajectories in the space of ϕ_2 and θ_3 for the case $\kappa_1 = \kappa_3 = 1$, $\kappa_2 = \kappa_4 = -1$. In figure 7(b) we plot the corresponding constant kinetic energy trajectories for a system of four Rankine vortices, for which the vorticity is constant and equal to $\pm 1/4r_v^2$ out to a distance, $r_v = 0.1a$, from the vortex centre and equal to zero for larger distance. The strengths of the vortices are then $\kappa_i = \pm 1$. The energy levels were calculated numerically (see Appendix C). In both plots, the energy levels have been shifted so that the maximum energy is zero. Apart from this, there is no renormalisation. It is reassuring to see that we obtain very similar results in the two cases. There is a single maximum at $\phi_2 = \theta_3 = \pi/2$, corresponding to the configuration we observe. This is consistent with the demonstration given by Dritschel (2020) that this is the only steady and stable configuration of two pair of point vortices of equal but opposite strength, in the case L = 0. That the configuration is stationary can intuitively be grasped by noting that the net motion of one vortex induced by the other three is zero. That the configuration

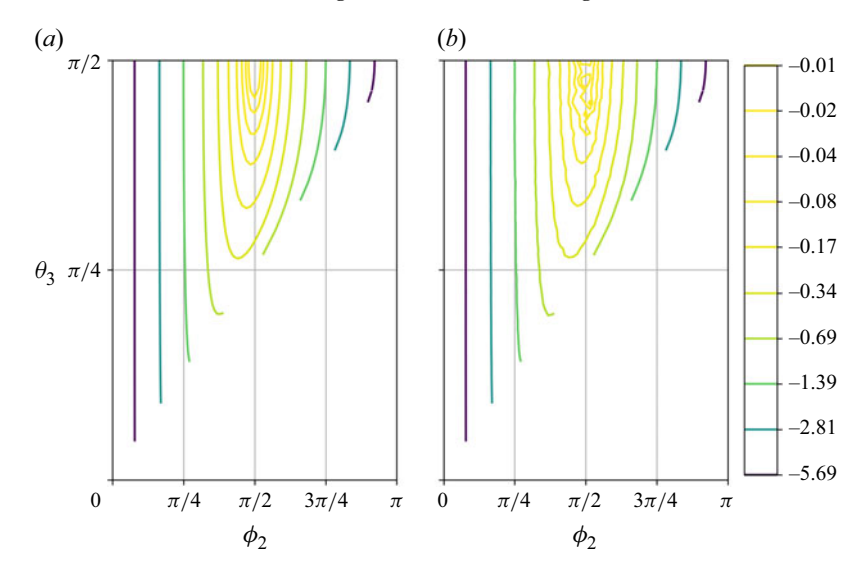


Figure 7. Constant energy trajectories for the four vortex system. (a) Interaction energy for four point vortices, calculated using the point vortex model. (b) Kinetic energy of four localised vortices, calculated numerically. The energy level has been shifted in both plots, so that the maximum energy is zero. Apart from this, the energy levels have not been renormalised.

is an energy extreme, may be intuitively grasped by regarding E as a potential energy of interaction.

Is there an interesting interpretation of this? First, it provides a clue to why the vortices are fixed in their configuration. They cannot move out from it, because that would decrease the energy of the system. Second, it may also provide a clue with deeper significance. In some sense, the flow seeks a maximum energy solution. This observation makes it very tempting to seek an explanation based on a statistical mechanics variational principle applied to an inviscid fluid, such as the maximum entropy principle (Robert 1991; Robert & Sommeria 1991). However, noting that the formation takes place under the action of a stochastic forcing, leading to a state with constant energy growth and almost constant enstrophy, it is difficult to see how such a principle can be applied. Enstrophy dissipation is a crucial element of the formation process. The configuration seems to be the one that maximises the energy for a given enstrophy. To prove or disprove this, we would need to investigate whether the observed field is the one of maximum energy out of all possible fields with a prescribed enstrophy, which seems to be an overwhelming task. To be more modest, we investigate if it is the maximum energy configuration out of all four point vortex configurations. To do this, we note that the sum of the squares of the strengths is an enstrophy measure. Strictly speaking, the mean enstrophy is infinite for a point vortex system if the strengths are finite. However, if we regard the vortices as Rankine vortices with constant vorticity out to a radius d, the mean enstrophy is proportional to $d^{-2}\sum_{i}\kappa_{i}^{2}$. For every finite d, the sum of the squares of the strengths will thus be an enstrophy measure. Thus, we numerically determine the maximum energy configuration of all configurations satisfying (3.5)–(3.7) and all combinations of κ_1 , κ_2 , κ_3 , κ_4 satisfying

$$\kappa_1 + \kappa_2 + \kappa_3 + \kappa_4 = 0, \tag{3.9}$$

$$\kappa_1^2 + \kappa_2^2 + \kappa_3^2 + \kappa_4^2 = 4. \tag{3.10}$$

For a given set of parameters κ_1 , κ_2 , θ_3 and ϕ_2 , the associated solutions of the vortex positions and strengths satisfying equations (3.5)–(3.7) and (3.9)–(3.10) were identified

and the energy was calculated by means of equation (3.8). The search in the 4-D space was first made by a random search algorithm to seek the highest local maximum, identified in the neighbourhood of the great circle configuration $\kappa_1 = 1$, $\kappa_2 = -1$, $\theta_3 = \pi/2$ and $\phi_2 = \pi/2$. After that, a numerical optimisation based on the Broyden–Fletcher–Goldfarb–Shanno algorithm was performed converging to the same maximum. Indeed, there is a single maximum configuration, which is exactly the configuration of four vortices of equal strength that we observe.

The fact that the configuration is an energy maximum, suggests that it will remain steady if the forcing is turned off. We have carried out two experiments to investigate this. In the first one, we took the full end state field of run 1 as the initial field. In the second one, we made an effort to initialise the field in such a way that it had a maximum degree of symmetry, by setting all modes for which l > 30 to zero as well as all remaining modes for which l = odd or l = even and $m \neq 2 + 4i$. In both cases, the configuration remained steady, however, with a spectacular difference that we cannot explain. In the first case, the great circle continued to rotate in a stationary solid body rotation around an axis in its own plane. In the second case, the flow remained completely steady.

3.3. Freely decaying simulations from random initial conditions

Dritschel, Oi & Marston (2015) undertook simulations of freely decaying 2-D turbulence on a sphere, leading to late time solutions with four coherent vortices, quite similar to the solutions we observe. The simulations were carried out to test statistical mechanics theories based on the 2-D Euler equation (Miller 1990; Robert 1991; Robert & Sommeria 1991), predicting that the solutions will relax to steady equilibrium states. The four vortices in the late time solutions reported by Dritschel et al. (2015) were of unequal strength and underwent unsteady oscillatory motions. They also reported evidence of small-scale vortices emerging in the flow fields at high resolution, and concluded that the flow remains persistently unsteady with no indications of relaxation to a steady state. Evidently, similar conclusions are not applicable to the end states of our forced simulations, which display a high degree of symmetry and steadiness. To explore the similarities between the solutions of our forced simulations and the late time solutions of decaying simulations, we have carried out three decaying simulations from random initial conditions with a prescribed energy spectrum. In runs 3 and 4, the initial spectrum is centred around $l_c = 8$, while the resolution is four times higher in run 4 compared with run 3. The initial conditions of run 3 and run 4 are not identical although the initial spectrum is the same, since the random phases are different in the initial fields. In run 5, the initial spectrum is centred around $l_c = 100.$

In figure 8, we see the evolution of mean energy and mean enstrophy from the three decaying runs. Time is measured in units $a/\sqrt{E_0}$, where E_0 is the initial mean energy which is set to unity, as is a. As seen in the figure, the energy is more or less constant in runs 3 and 4, implying that there is essentially no energy dissipation at all in these runs, while there is some energy dissipation early in run 5, reflecting the fact that it is initialised with a spectrum peaking at $l_c = 100$. In all three runs, the flow relaxes to a state in which mean enstrophy, as well as mean energy, can be regarded as constant. In figure 9(a,b), we see the evolution of the energy spectra from runs 4 and 5. In the early stage of run 4, the initial spectrum centred at $l_c = 8$, broadens to a wide spectrum of the form $E(l) \sim l^{-3}$, in accordance with the prediction of Kraichnan (1967) for the forward enstrophy cascade. This is clearly seen at t = 15. In a corresponding way, the initial spectrum in run 5, centred at $l_c = 100$, broadens to a wide spectrum peaking at l < 10. This broadening is caused by the inverse energy cascade. For comparison, we have added a line with slope -5/3,

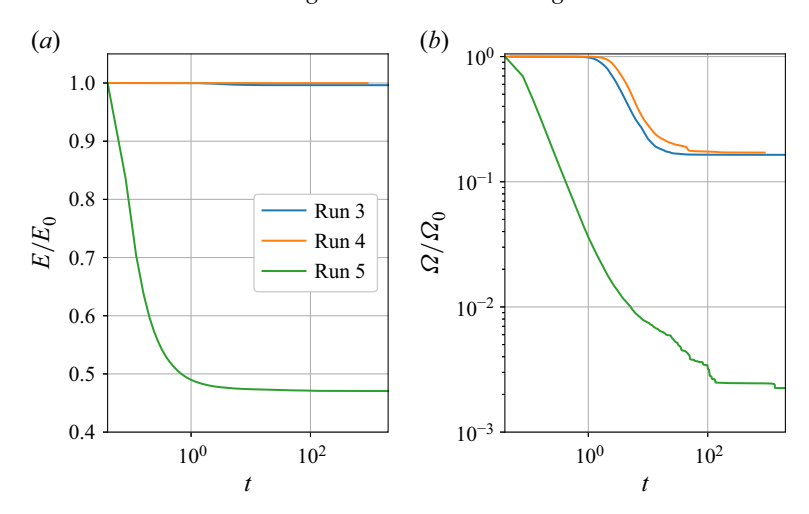


Figure 8. Evolution of (a) mean energy and (b) enstrophy from runs 3, 4 and 5.

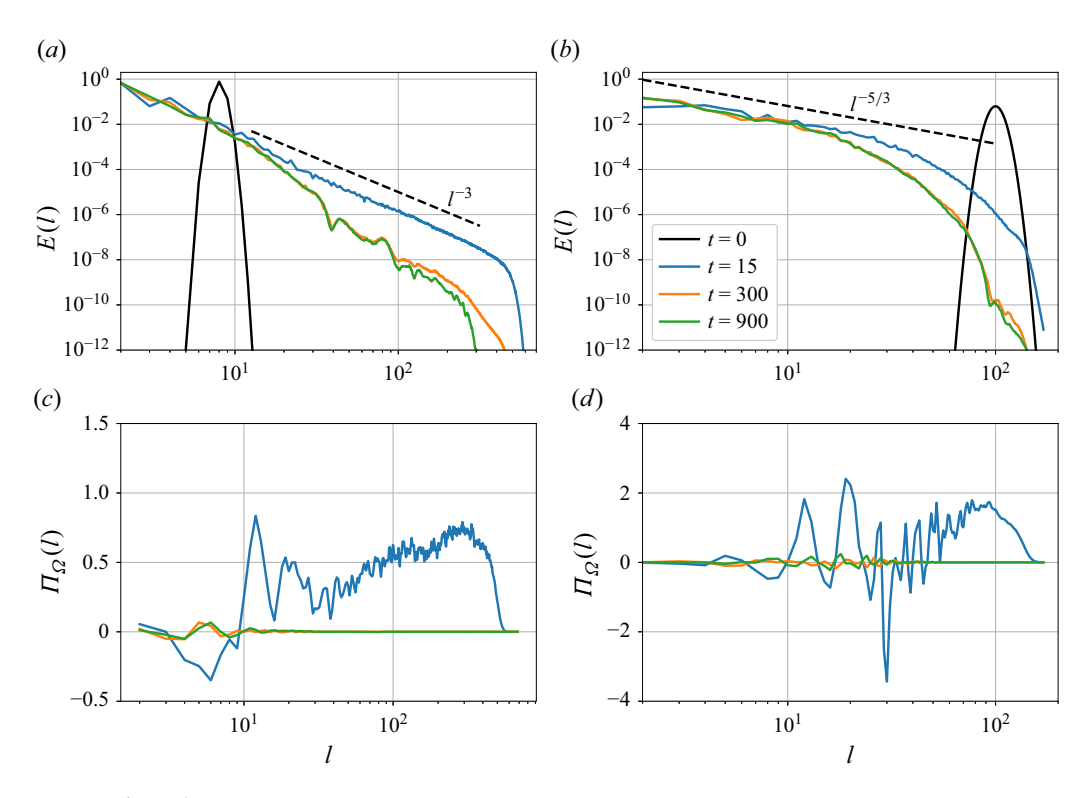


Figure 9. Energy spectra from (a) run 4, (b) run 5. Enstrophy fluxes from (c) run 4, (d) run 5.

although it is unclear if the spectrum conforms to this shape. In figure 9(c,d), we see the spectral enstrophy flux from the same runs. Using the value $\Pi_{\Omega}=0.5$ and fitting the spectrum in run 4 at t=15 to $E(l)=K\Pi_{\Omega}^{2/3}l^{-3}$ we obtain $K\approx 2$, not too far from K=1.3, as found by Lindborg & Alvelius (2000) in Fourier space. At late times, the spectra approach a steady shape and the enstrophy fluxes become very small. The late

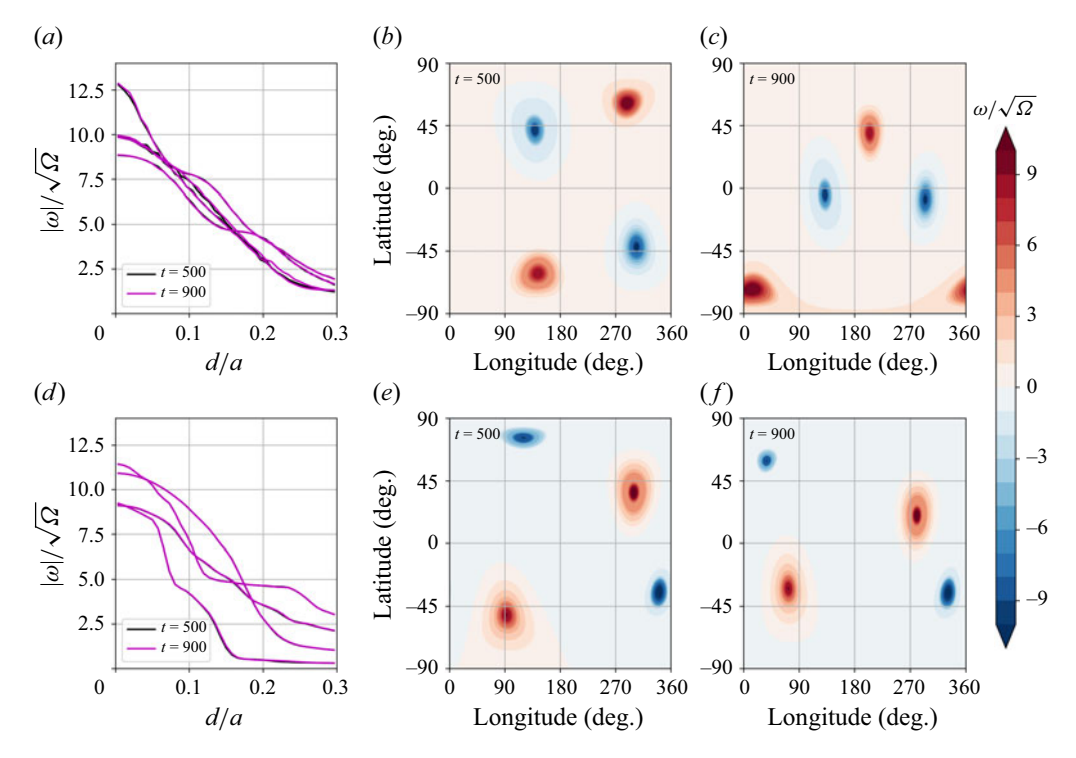


Figure 10. Normalised mean vorticity as function of normalised distance from the vortex centre and vorticity fields at t = 500 and t = 900 from (a-c) run 3 and (d-f) run 4. In (d) the profiles at t = 500 (black) and t = 900 (magenta) are indistinguishable.

time solutions are similar to the late time solutions of Dritschel *et al.* (2015), exhibiting four coherent vortices.

In figure 10, we see the vorticity profiles for the four vortices and the vorticity fields at t = 500 and t = 900 from runs 3 and 4. The profiles are computed as the average vorticity along a circle with distance d from the vortex centre. In both cases, there are no signs of other vortices in the field and the profile of each vortex has not changed in the time span $t \in [500, 900]$. In the higher resolved run, the profiles at t = 500 and t = 900 are completely indistinguishable. The field consists of four persistent vortices that are slowly advected over the sphere, without any changes in their internal structure. Unlike the forced simulations, the four vortices are not of equal strength. They are wider and less symmetric. Some of the profiles are step-like, as also found by Dritschel $et\ al.\ (2015)$.

In figure 11, we see time series of the geodesic distances between like signed, d^{++} and d^{--} , and opposite signed vortices, d^{+-} , from runs 3 and 4. In both cases, the distances undergo periodic motions that are in phase. In run 3, the period of d^{+-} is half the period of d^{++} and d^{--} . In run 4, it is the other way around. The motions bear every sign of a dynamical system with a few degrees of freedom, possibly a single one, as in the four point vortex model. It is noteworthy that the configuration is not very far from lying on a great circle in run 3, where the amplitudes of the motions are quite small, while the configuration is further away from a great circle in run 4, where the amplitudes are larger. Interpreting these results in the light of the four point vortex model, the configuration in run 3 is closer to the energy maximum of the four vortex system than the configuration in run 4. We can conclude that increased resolution does not move us closer to the maximum.

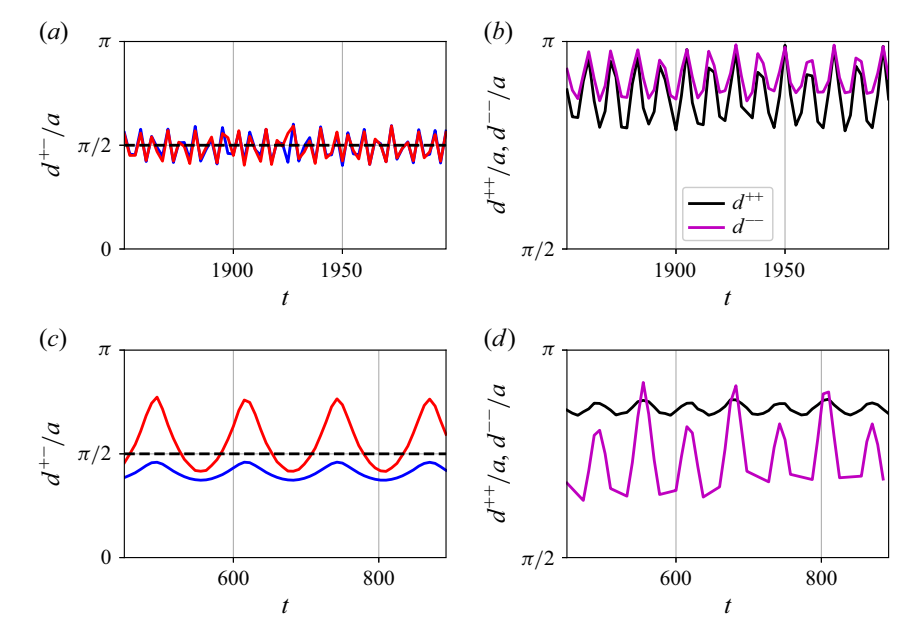


Figure 11. Normalised geodesic distances between vortex centres versus time. Distances between opposite signed vortices denoted as d^{+-}/a and distances between like signed vortices denoted as d^{++}/a and d^{--}/a . (a,b) Run 3, (c,d) run4.

The theory of Robert (1991) and Robert & Sommeria (1991) predicts that solutions to the Euler equations will relax to states in which there is a functional relation between the vorticity and the streamfunction. Such states are stationary solutions to the Euler equations, since $\mathbf{u} \cdot \nabla \omega \equiv 0$, when $\omega = F(\psi)$. The prediction can be tested by making a scatter plot of (ψ, ω) . If all points fall on the same line, there is a functional dependence, otherwise not. In figure 12, we present such plots from the forced simulations, run 1 and run 2, and the decaying simulations, run 3 and run 4.

The plot where the points are closest aggregated in the vicinity of a single line is the one from run 1. There are two branches of high and low vorticity, where we see two distinctive lines representing the four vortex cores. Apparently, the vortex cores are very stable. At lower values of vorticity, the points do not fall onto a single line but onto a broader band. The plot from run 2 is similar to the plot from run 1, with some differences. The two main branches of high and low vorticity are steeper and contain higher magnitude values. This difference is a reflection of the fact that the vortices in run 2 are more narrow than in run 1. A close inspection of the two main branches in run 2 reveals that each of them is divided into two sub-branches, corresponding to two vortices of positive/negative sign. This is particularly clear if we look at the negative branch. At lower values of vorticity, the band in which the points aggregate is somewhat broader in run 2 than in run 1. These differences can be attributed to the fact that the effective time span of condensation was longer in run 1 than in run 2. A continuation of run 2 would probably result in a scatter plot coming closer to a stationary solution. We conclude that the condensate is formed in a close vicinity of a stationary solution to the unforced Euler equation.

In the decaying simulations, the points fall onto four branches of bands, corresponding to the four vortices. That fact that the bands have limited width can be interpreted as a sign of a relatively high degree of local stationarity, while the fact that the bands are separated can be interpreted as a reflection of global unsteadiness. The difference between

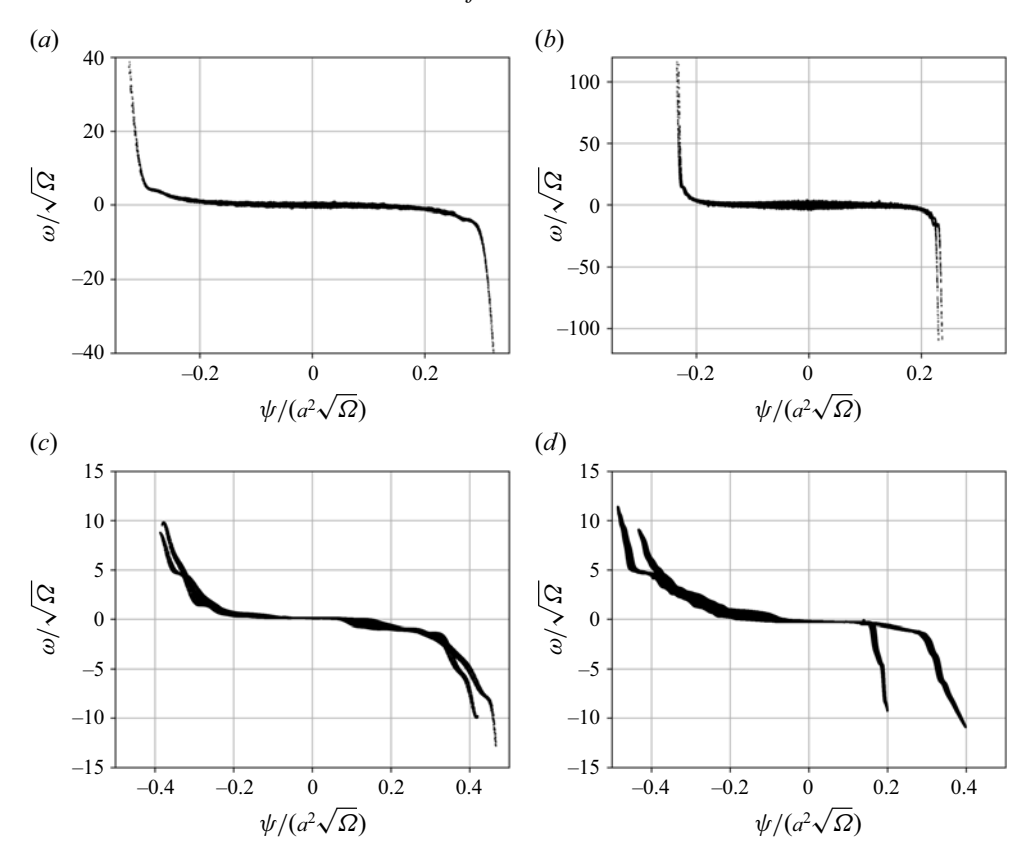


Figure 12. Scatter plots of (ω, ψ) from the end states of (a) run 1, (b) run 2, (c) run 3, (d) run 4.

the structure of the two plots from run 3 and run 4 can be attributed to the difference in the initial conditions. Our plots are similar to the corresponding plots of Dritschel *et al.* (2015) (see their figure 12), with an important difference. Dritschel *et al.* (2015) used two different numerical methods, denoted as Geodesic Grid Method and Combined Lagrangian Advection Method. Using the second method, they found that the scatter plot (their figure 12b) exhibited a thin mist of points structured in vertical lines, falling outside the main branches, while the scatter plot of the first method (their figure 12a) did not show any such feature. Putting a high degree of confidence in the second method, Dritschel *et al.* (2015) interpreted this feature as evidence of a multitude of small-scale vortices emerging with increased resolution. Since none of our plots show any such feature, we are sceptical to this interpretation. We see no signs of small-scale vortices emerging with increased resolution in our scatter plots, in our plots of the vorticity fields in physical space or in spectral space.

We now turn our attention to our last simulation, run 5, that was carried out mainly to investigate if a field that is initialised with a spectrum centred at a large wavenumber $(l_c = 100)$ will display a late time solution consisting of four localised vortices. The answer is yes, although we had to run the simulation for a very long time to confirm this. In figure 13, we see how the vorticity field develops over time as we run the simulation. A multitude of vortices are formed at a quite early time in the simulation. Their number is subsequently reduced as they interact in a random way and undergo vortex pairings. In the end, there are four vortices of unequal strength undergoing periodic motions. In figure 14,

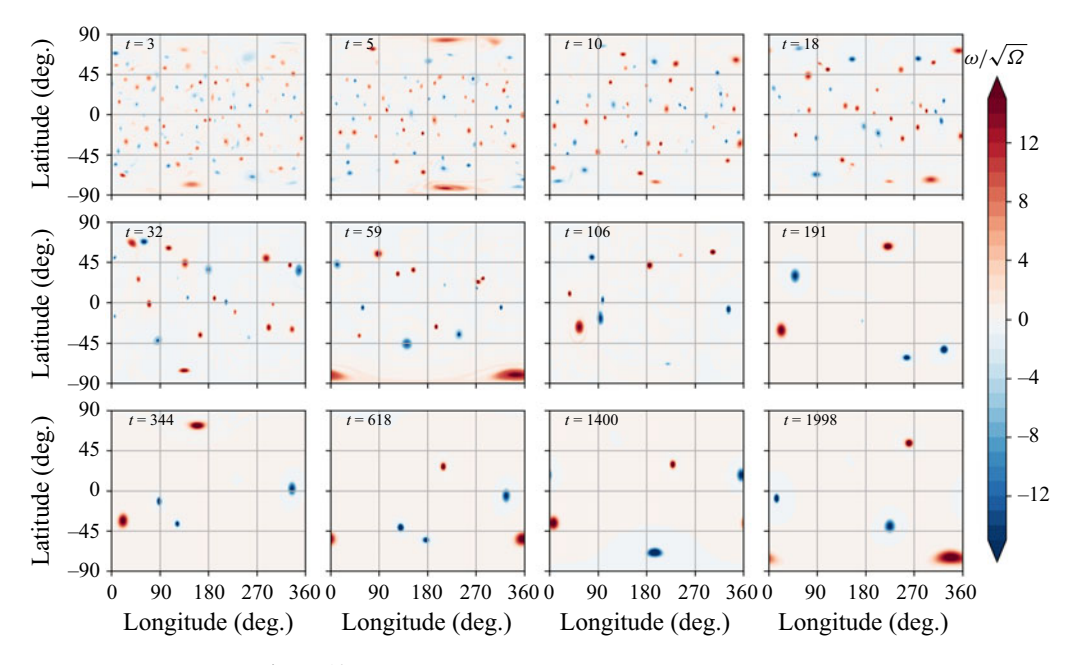


Figure 13. Evolution of the vorticity field over time in run 5.

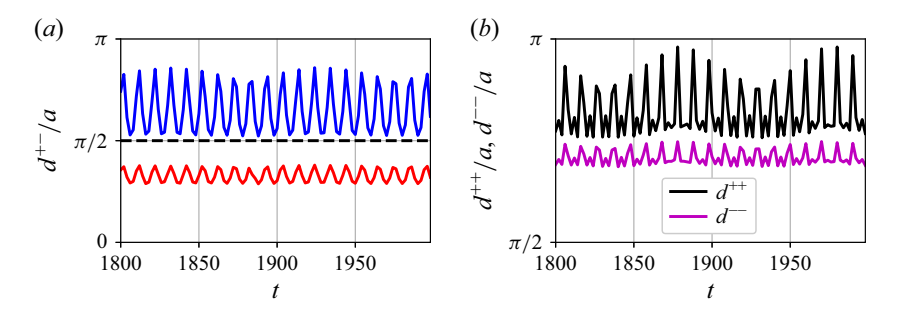


Figure 14. Geodesic distances between two vortex centres versus time, from run 5, plotted in the same way as in figure 11.

we see the motions of the geodesic distances between the vortices, plotted in a similar way as in figure 11. Again, we see regular periodic motions that are in phase, but the pattern is a little bit more complex than in runs 3 and 4. The main period of the modulations in d^{+-} is the same as the main period of the modulations in d^{++} and d^{--} . There is also a period of smaller amplitude modulations in d^{++} and d^{--} which is just as long. On top of this, there is a longer period that is modulating the magnitude of the peaks. A future study will reveal if these motions can be described by the four point vortex model with a single degree of freedom.

4. Conclusions

Our simulations of forced 2-D turbulence on a sphere confirm the prediction by Kraichnan (1967) that the flow generated by a 2-D inverse energy cascade undergoes something like a phase transition, from a chaotic to an ordered state, when the cascade reaches the scale of the confinement. The condensation process on a sphere is similar to the process on a plane, with the important difference that the condensate forms as four coherent vortices on

a sphere, whereas it forms as two vortices on a plane. We find that the width of the vortices is set by the forcing scale, implying that the vortices will approach the point vortex limit in the limit of very-small-scale forcing. Most likely, this is true also for the condensate on a 2π -periodic square, and the k^{-3} -spectrum that is observed in such simulations is probably a reflection of this. While the formation of two equal vortices of opposite sign on a plane may seem to be a straightforward consequence of the fact that mean vorticity must remain zero, the formation of the condensate on a sphere seems more mysterious. It is quite remarkable that the four vortices are of equal strength and that they arrange themselves on a great circle which moves over the sphere under the influence of the random forcing. These observations call for an explanation. Tentatively, we suggest that the symmetric configuration of the vortices may be explained by a maximum energy principle. The late time inverse energy cascade proceeds through a process in which the flow increases its energy, without notably increasing its enstrophy, by reducing the number of vortices to a minimum by vortex mergers and by finding the optimal distribution of vortex strengths as well as the optimal vortex configuration in physical space.

The late time solutions of our freely decaying simulations also exhibit four coherent vortices, similar to the condensate, with a quite high degree of steadiness. However, there are important differences between the forced and the decaying simulations. The vortices in the decaying simulations are not generally of equal strength and they do not arrange themselves on a great circle. The vortex configuration undergoes regular periodic motions, indicative of a dynamical system with a few degrees of freedom, possibly the four point system with a single degree of freedom. However, increased resolution does not move us closer to the stationary energy maximum of the condensate. Since there is essentially no dissipation of enstrophy in the late time solutions, the periodic motions would persist indefinitely, or nearly so, if we continued the simulations. We can therefore conclude that the prediction of statistical mechanics theories (Miller 1990; Robert 1991; Robert & Sommeria 1991) of a relaxation to a steady state does not hold. In this respect, we draw the same conclusion as Dritschel et al. (2015). Nevertheless, we find that the late time solutions show a very high degree of steadiness and regularity. We find no evidence suggesting that these solutions are chaotic. The existence of non-chaotic periodic solutions does not seem to be an insurmountable obstacle to further developments of statistical mechanics theories based on the Euler equation. The main challenge to such theories is to reconcile them with fact that the late time solutions are reached in a process in which enstrophy dissipation is a key element. Without enstrophy dissipation, the enstrophy cascade would go on indefinitely to finer and finer scales, and the solutions would never approach non-chaotic states. This is true for the decaying as well as the forced simulations.

There is a certain feature of the formation process that was not explicitly predicted by Kraichnan (1967) but is implicitly suggested by the term 'condensate'. The order is not only established at the largest scales of motion, but also at smaller scales, all the way down to the forcing scale. The condensate is first formed as an ordered symmetric state at l < 10. The symmetry is subsequently established at l > 10. The four vortex system then acts as a global attractor which is effectively absorbing the energy and dissipating virtually all the enstrophy that is injected by the small-scale stochastic forcing. The energy and enstrophy fluxes are maintained by highly non-local interactions, suggesting that condensation may be modelled as a process in which a huge number of micro-vortices align into a global pattern. In the end state, the random component of the flow is close to zero, even at the small scales. Indeed, the process is a beautiful example of self-organisation.

Acknowledgements. The authors would like to thank D. Dritschel and A. Nordmark for fruitful interactions. Four anonymous reviewers are acknowledged for constructive criticism. Finally, E.L. would like to pay tribute

to Eudoxus of Cnidus (390-340 B.C.), whose model of the solar system as a mechanical system of rotating spheres has been a great source of inspiration.

Funding. The computations were enabled by resources provided by the National Academic Infrastructure for Supercomputing in Sweden (NAISS) through the project grant NAISS-2024/22-397.

Declaration of interests. The authors declare no conflict of interest.

Appendix A. Energy spectrum of two point vortices on a plane

In this appendix, we show that the energy spectrum of two point vortices on a plane with periodic boundary conditions has the form $E(k) \sim k^{-3}$ and that the energy is zero in half of the modes. We consider a field of two point vortices in a 2π -periodic domain

$$\omega(x, y) = (2\pi)^2 \omega_0 [\delta(x - \pi/2, y - 3\pi/2) - \delta(x - 3\pi/2, y - \pi/2)].$$
 (A1)

We expand the vorticity field in a Fourier series

$$\omega(x, y) = \sum_{k_x, k_y} \hat{\omega}(k_x, k_y) \exp[i(k_x x + k_y y)], \tag{A2}$$

$$\hat{\omega}(k_x, k_y) = \frac{1}{(2\pi)^2} \int \int \omega(x, y) \exp\left[-i(k_x x + k_y y)\right] dx dy, \tag{A3}$$

where k_x and k_y are positive or negative integers. The enstrophy distribution in Fourier space can then be calculated as

$$\Omega(k_x, k_y) = \frac{1}{2}\hat{\omega}\hat{\omega}^* = \omega_0^2 \left\{ 1 - \cos[(k_x - k_y)\pi] \right\}.$$
 (A4)

It is equal to zero if $k_x + k_y =$ even, and equal to $2\omega_0^2$ if $k_x + k_y =$ odd. Passing to the limit of a continuous enstrophy spectrum, $\Omega(k)$, where k is the magnitude of the wavenumber vector (see Kraichnan 1967), we have

$$\Omega(k) = \frac{\Omega(k_x, k_y)}{4\pi k},\tag{A5}$$

where we have divided by $4\pi k$ instead of $2\pi k$ to account for the fact that half the modes are zero. The corresponding energy spectrum is then

$$E(k) = k^{-2}\Omega(k) = \frac{\omega_0^2}{4\pi}k^{-3}.$$
 (A6)

Appendix B. Number of degrees of freedom for the four point vortex system with zero angular momentum

In this appendix, we formalise the symmetry argument given in § 3.2, showing that the four point vortex system with zero angular momentum has a single degree of freedom. We transform the equations of motion to a frame rotating with angular velocity $\Omega(t)$, that is allowed to vary in both magnitude and direction. The equations of motion (3.2) are transformed as

$$\boldsymbol{u}_{j}' = \boldsymbol{u}_{j} + \boldsymbol{n}_{j} \times \boldsymbol{\Omega} = \sum_{i} \kappa_{i} \frac{\boldsymbol{n}_{i} \times \boldsymbol{n}_{j}}{1 - \boldsymbol{n}_{i} \cdot \boldsymbol{n}_{j}} + \boldsymbol{n}_{j} \times \boldsymbol{\Omega} , \qquad (B1)$$

where u'_j is the velocity of the *j*th vortex in the rotating frame. The transformed equations still conserve E, as defined in (3.4), which is clear from the fact that E is only a function

of the geodesic distances between the vortices. We can also show this explicitly

$$\frac{\mathrm{d}E}{\mathrm{d}t}|_{rot} = \sum_{i \neq j} \frac{\kappa_i \kappa_j}{1 - \mathbf{n}_i \cdot \mathbf{n}_j} \left(\mathbf{n}_i \cdot \frac{\mathrm{d}\mathbf{n}_j}{\mathrm{d}t}|_{rot} + \mathbf{n}_j \cdot \frac{\mathrm{d}\mathbf{n}_i}{\mathrm{d}t}|_{rot} \right)$$

$$= \sum_{i \neq j} \frac{\kappa_i \kappa_j}{1 - \mathbf{n}_i \cdot \mathbf{n}_j} \left(\mathbf{n}_i \cdot \frac{\mathrm{d}\mathbf{n}_j}{\mathrm{d}t} + \mathbf{n}_i \cdot (\mathbf{n}_j \times \mathbf{\Omega}) + \mathbf{n}_j \cdot \frac{\mathrm{d}\mathbf{n}_i}{\mathrm{d}t} + \mathbf{n}_j \cdot (\mathbf{n}_i \times \mathbf{\Omega}) \right)$$

$$= \sum_{i \neq j} \frac{\kappa_i \kappa_j}{1 - \mathbf{n}_i \cdot \mathbf{n}_j} \frac{\mathrm{d}(\mathbf{n}_i \cdot \mathbf{n}_j)}{\mathrm{d}t} = \frac{\mathrm{d}E}{\mathrm{d}t} = 0, \tag{B2}$$

where we have used $\mathbf{n}_i \cdot (\mathbf{n}_j \times \mathbf{\Omega}) + \mathbf{n}_j \cdot (\mathbf{n}_i \times \mathbf{\Omega}) = 0$. It should be pointed out that E should still be interpreted as the energy in the inertial frame. In other words, the energy in the inertial frame is conserved by the equations of motion in the rotating frame. The angular momentum equation is transformed as

$$\frac{\mathrm{d}\boldsymbol{L}}{\mathrm{d}t}|_{rot} = \frac{\mathrm{d}\boldsymbol{L}}{\mathrm{d}t} + \boldsymbol{L} \times \boldsymbol{\Omega} = \boldsymbol{L} \times \boldsymbol{\Omega} , \qquad (B3)$$

where L is the absolute angular momentum in the inertial frame. If L = 0, the absolute angular momentum is conserved in the rotating frame.

Fix the position of the first vortex in the rotating frame, so that $u'_1 = 0$. This determines two components of Ω in terms of u_1 – the components that are perpendicular to n_1 . Constrain the motion of the second vortex so that it has only a single degree of freedom in the rotating frame. This determines the component of Ω that is parallel to n_1 . For example, fix the first vortex at the north pole and the second vortex at a certain latitude in the rotating frame. Express the velocities of the first and second vortex in the inertial frame as

$$u_1 = u_1 e_x + v_1 e_y + w_1 e_z$$
, $u_2 = u_2 e_x + v_2 e_y + w_2 e_z$, (B4)

where (x, y, z) is a Cartesian system that is fixed in the rotating frame. Then write

$$\mathbf{n}_1 = \mathbf{e}_z$$
, $\mathbf{n}_2 = \cos \theta_2 \mathbf{e}_z + \sin \theta_2 \mathbf{e}_x$, (B5)

where θ_2 is the colatitude of the second vortex. This determines Ω as

$$\mathbf{\Omega} = -v_1 \mathbf{e}_x + u_1 \mathbf{e}_y + \frac{v_2 - \cos \theta_2 v_1}{\sin \theta_2} \mathbf{e}_z.$$
 (B6)

Insert this expression into (B1). In this way, we obtain a coupled set of equations for five coordinates, one specifying the position of the second vortex and the other four the positions of the third and fourth vortices in the rotating frame. We have thus eliminated three degrees of freedom. The conservation laws provide four holonomic constraints, because they hold in the rotating frame. Thus, the system has a single degree of freedom.

Appendix C. Maximum energy for a configuration of four localised vortices

In this appendix, we describe how the constant energy trajectories in figure are calculated. We assume that the vorticity for each vortex is constant for $d \le 0.1a$, where d is the geodesic distance from the vortex centre. For d/a > 0.1 we set the vorticity to zero. All vortices have the same strength. Vortices 1 and 3 are positive and vortices 2 and 4 are negative. We represent the vorticity field as a truncated spherical harmonic expansion

$$\omega(\theta, \phi) = \sum_{l=1}^{682} \sum_{m=-l}^{l} \omega_l^m Y_l^m(\theta, \phi).$$
 (C1)

We let (θ_i, ϕ_i) , i = 1, 2, 3, 4 be the positions of the four vortex centres. Without loss of generality we set $\theta_1 = \theta_2 = \pi/2$ and $\phi_1 = 0$. If our vortices are regarded as point vortices, the constraint L = 0 provides three equations relating the remaining five angles, ϕ_2 , θ_3 , ϕ_3 , θ_4 and ϕ_4 , which are equations (3.5)–(3.7) with $\kappa_1 = \kappa_3 = 1$ and $\kappa_2 = \kappa_4 = -1$. In the case of localised vortices with $d/a \ll 1$, these conditions can be assumed to hold to a high degree of accuracy. These constraints are equivalent to constraining the three spherical harmonic modes with l = 1 to be zero. We use these constraints and calculate the mean energy over all configurations numerically, by varying ϕ_2 and θ_3 . In figure 7(b), the constant energy trajectories are displayed.

REFERENCES

- BOER, G.J. 1983 Homogeneous and isotropic turbulence on the sphere. J. Atmos. Sci. 40, 154-163.
- BOFFETTA, G., CELANI, A. & VERGASSOLA, M. 2000 Inverse energy cascade in two-dimensional turbulence: deviations from Gaussian behavior. *Phys. Rev. E* **61** (1), R29–R32.
- CHEN, S., ECKE, R.E., EYINK, G.L., RIVERA, M., WAN, M. & XIAO, Z. 2006 Physical mechanism of the two-dimensional inverse energy cascade. *Phys. Rev. Lett.* **96** (8), 084502.
- CHERTKOV, M., CONNAUGHTON, C., KOLOKOLOV, I. & LEBEDEV, V. 2007 Dynamics of energy condensation in two-dimensional turbulence. *Phys. Rev. Lett.* **99** (8), 084501.
- CHO, J.Y.-K. & POLVANI, L.M. 1996 The emergence of jets and vortices in freely evolving, shallow-water turbulence on a sphere. *Phys. Fluids* **8** (6), 1531–1552.
- DRITSCHEL, D.G. 2020 Equilibria and stability of four point vortices on a sphere. *Proc. R. Soc. A* 476, 20200344.
- DRITSCHEL, D.G. & BOATTO, S. 2015 The motion of point vortices on closed surfaces. Proc. R. Soc. A 471, 20140890.
- DRITSCHEL, D.G., QI, W. & MARSTON, J.B. 2015 On the late-time behaviour of a bounded, inviscid twodimensional flow. J. Fluid Mech. 783, 1–22.
- EYINK, G.E. & SREENIVASAN, K.R. 2006 Onsager and the theory of hydrodynamic turbulence. Rev. Mod. Phys. 78, 87–135.
- FJØRTOFT, R. 1953 On the changes in the spectral distribution of kinetic energy for twodimensional, nondivergent flow. *Tellus* 5 (3), 225–230.
- FRIGO, M. & JOHNSON, S.G. 2005 The design and implementation of FFTW3. *Proc. IEEE* **93** (2), 216–231. GILBERT, A.D., RIEDINGER, X. & THUBURN, J. 2014 On the form of the viscous term for two dimensional Navier–Stokes flows. *Q. J. Mech. Appl. Maths* **67** (2), 205–228.
- ISHIOKA, K. 2018 A new recurrence formula for efficient computation of spherical harmonic transform. J. Meteorol. Soc. Jpn Ser. II 96 (2), 241–249.
- KOLOKOLOV, I.V. & LEBEDEV, V.V. 2016 Structure of coherent vortices generated by the inverse cascade of two-dimensional turbulence in a finite box. *Phys. Rev. E* **93**, 033104.
- KRAICHNAN, R.H. 1967 Inertial ranges in two-dimensional turbulence. Phys. Fluids 10 (7), 1417.
- KRAICHNAN, R.H. 1971 Inertial-range transfer in two-and three-dimensional turbulence. J. Fluid Mech. 47 (3), 525–535.
- KRISHNAMURTI, T.N., BEDI, H.S., HARDIKER, V. & WATSON-RAMASWAMY, L. 2006 An Introduction to Global Spectral Modeling, vol. 35. Springer Science & Business Media.
- LINDBORG, E. & ALVELIUS, K. 2000 The kinetic energy spectrum of the two-dimensional enstrophy turbulent cascade. *Phys. Fluids* **12** (5), 945–947.
- LINDBORG, E. & NORDMARK, A. 2022 Two-dimensional turbulence on a sphere. J. Fluid Mech. 933, A60.
- MILLER, J. 1990 Statistical mechanics of Euler equations in two dimensions. Phys. Rev. Lett. 45, 2137-2140.
- MUSACCHIO, S. & BOFFETTA, G. 2019 Condensate in quasi-two-dimensional turbulence. *Phys. Rev. Fluids* 4 (2), 022602.
- PEYRET, R. 2002 Spectral Methods for Incompressible Viscous Flow, vol. 148. Springer.
- POLVANI, L.M. & DRITSCHEL, D.G. 1993 Wave and vortex dynamics on the surface of a sphere. *J. Fluid Mech.* 255, 35–64.
- ROBERT, R. 1991 A maximum-entropy principle for two-dimensional perfect fluid dynamics. J. Stat. Phys. 65, 531–553.
- ROBERT, R. & SOMMERIA, J. 1991 Statistical equilibrium states for two-dimensional flows. J. Fluid Mech. 229, 291–310.

- SILBERMAN, I. 1954 Planetary waves in the atmosphere. J. Meteorol. 274, 27–34.
- SMITH, L.M. & YAKHOT, V. 1994 Finite-size effects in forced two-dimensional turbulence. *J. Fluid Mech.* 274, 115–138.
- TANG, C.-M. & ORSZAG, S.A. 1978 Two-dimensional turbulence on the surface of a sphere. *J. Fluid Mech.* 87, 305–319.